

Rhythmic production of consonant-vowel syllables synchronizes traveling waves in speech-processing brain regions

Joaquín Rapela*

May 5, 2017

Abstract

Nature is abundant in oscillatory activity, with oscillators that have the remarkable ability of synchronizing to external events. Using electrocorticographic (**ECoG**) recordings from a subject rhythmically producing consonant-vowel syllables (**CVSs**) we show that neural oscillators recorded at individual **ECoG** electrodes become precisely synchronized to initiations of the production of **CVSs** (i.e., that these initiations occur at precise phases of bandpassed-filtered voltages recorded at most **ECoG** electrodes). This synchronization is not a trivial consequence of the rhythmic production of **CVSs**, since it takes several minutes to be fully established and is observed at the frequency of **CVS** production and at its second harmonic. The phase of filtered voltages at which **CVSs** are produced varies systematically across the grid of electrodes, consistently with the propagation of traveling waves (**TWs**). Using these synchronized phases we isolate a first **TW** in voltages (filtered at the median **CVS**-production frequency) moving from primary auditory to premotor cortex, and a second **TW** in high-gamma amplitude (coupled to phase at the **CVS**-production frequency) moving along the same path but in opposite direction. To our knowledge, this is the first report of rhythmic motor acts synchronizing spatio-temporally organized cortical activity in the human brain.

*rapela@ucsd.edu

Contents

1	Introduction	1
2	Results	2
2.1	Synchronization of models of single-neuron oscillators to periodic input pulses	2
2.1.1	1-to-1 synchronization at the fundamental frequency	2
2.1.2	2-to-1 synchronization at the second harmonic	2
2.2	Synchronization of neural populations to rhythmically produced CVSs	2
2.2.1	1-to-1 synchronization at the fundamental frequency	3
2.2.2	2-to-1 synchronization at the second harmonic	3
2.3	Synchronization of traveling waves to rhythmically produced consonant-vowel syllables	4
2.3.1	Synchronization of oscillators across electrodes	4
2.3.2	TWs between premotor and primary auditory cortex synchronized to the production of CVSs	4
3	Discussion	5
4	Methods	5
4.1	Oscillator models	5
4.2	Measuring CVS phases	5
4.3	Circular statistics concepts	6
4.4	PLI	6
5	Acknowledgments	6

1 Introduction

Physiological function emerges from interactions of neurons with each other and with external inputs to generate rhythms essential to life (Glass, 2001). The heartbeat results from interactions of thousand of pacemaker cells in the right atrium of the heart (DeFelice and Isaac, 1993; Guevara and Lewis, 1995). Nerve cells generating locomotion respond with precise phase relation depending on the type of gait (Golubitsky et al., 1999). And the sleep-wake rhythm is usually synchronized to the light-dark cycle (Winfree, 2001; Strogatz, 1986). Physiological oscillations can be synchronized to appropriate external or internal stimuli. Plants and animals show a circadian rhythm in which key processes show a 24-hour periodicity, which is usually set by the 24-hour light-dark cycle. Thus, the dark-light cycle synchronizes the intrinsic rhythm of plants and animals (Winfree, 2001; Strogatz, 1986). Periodic inputs from medical devices can synchronize functions of the body. For example, a mechanical ventilator delivers mixes of gases to patients in a periodic fashion. The resulting lung inflation interacts with the patient’s intrinsic respiratory rhythms so that the patient respiratory rhythm is entrained to the ventilator (Petrillo and Glass, 1984; Graves et al., 1986; Simon et al., 2000).

External visual (Regan, 1966) and auditory (Galambos et al., 1981) rhythmic stimuli entrain brain oscillations (i.e., drag brain oscillations to follow the rhythm of the stimuli), and this entrainment is modulated by attention so that the occurrence of attended stimuli coincides with the phase of brain oscillations of maximal excitability (Lakatos et al., 2005, 2008, 2013; O’Connell et al., 2011; Besle et al., 2011; Gomez-Ramirez et al., 2011; Zion Golumbic et al., 2013; Cravo et al., 2013; Mathewson et al., 2010; Spaak et al., 2014; Gray et al., 2015). Although speech is only quasi rhythmic (Cummins, 2012) an increasing number of studies is showing that neural oscillations can entrain to speech sound (e.g., Zion Golumbic et al., 2013; Gross et al., 2013; Doelling et al., 2014; Millman et al., 2015; Park et al., 2015). For recent reviews on the entrainment of neural oscillations to speech sound see Peelle and Davis (2012); Zion Golumbic et al. (2012); Ding and Simon (2014).

What is currently unknown is whether rhythmic motor acts can synchronize neural oscillators. In a previous article (Rapela, 2016) we reported that rhythms in electrocorticographic (ECoG) recordings from speech processing brain regions in the left hemisphere of a subject rhythmically producing consonant-vowel syllables (CVSs) are spatio-temporally organized as traveling waves (TWs). We also showed that the coupling between phase at the CVS-production frequency and amplitude in the high-gamma range was spatially organized in agreement with the propagation of TWs. Here we demonstrate that the previously reported TWs become precisely synchronized to the production of CVSs.

The synchronization of neural oscillators to rhythmic inputs can (1) be precise, (2) take time to develop, and (3) operate on oscillators at different temporal scales (Arnold tongues; Izhikevich, 2007, Chapter 10). To motivate our findings in ECoG recordings, in Section 2.1 we illustrate these synchronization concepts in models of single-neuron oscillators. In Section 2.2 we show that the synchronization of neural oscillators over speech production regions (1) is precise, (2) takes time to develop, and (3) operates on oscillators at the median frequency of CVS production and at its second harmonic. Section 2.3.1 shows that the phases of filtered voltages at which CVSs are initiated (i.e., the CVS phases) vary systematically across the grid of ECoG electrodes, consistently with the propagation of TWs. Using these synchronized phases in Section 2.3.2 we isolate a first TW synchronized to the production of CVSs in voltages filtered around the median CVS-production frequency and moving from premotor to auditory cortex, and a second TW, also synchronized to the production of CVS, but in high-gamma amplitude coupled with phase at the median CVS-production frequency, and traveling along the same path but in opposite direction as the previous TW.

2 Results

2.1 Synchronization of models of single-neuron oscillators to periodic input pulses

In this section we illustrate how simulated oscillators receiving periodic inputs (stimulation frequency $f_s = 0.15$ Hz) can synchronize to these inputs. We first demonstrate a 1-to-1 synchronization (i.e., one oscillator cycle paired to one input) of an oscillator with a natural oscillation frequency close to the stimulation frequency (Section 2.1.1). Next we exemplify a 2-to-1 synchronization (two oscillator cycles paired to one input) of an oscillator with a natural frequency at the second harmonic of the stimulation frequency (Section 2.1.2).

2.1.1 1-to-1 synchronization at the fundamental frequency

Figures 1 and 2 show the membrane potential of an oscillator (blue trace) with natural frequency close to the stimulation frequency (see Slower Oscillator in Section 4.1) and its periodic current pulses inputs (gray vertical lines with scale on the right axis) at the beginning of the stimulation period and after 150 seconds of stimulation, respectively. At the beginning of the stimulation the oscillator is not synchronized to its inputs (Figure 1), but after 150 seconds it is already synchronized (Figure 2). Figure 2 illustrates 1-to-1 synchronization in an oscillator whose natural oscillation frequency is close to the stimulation frequency. Figure 3 plots phases of the oscillatory cycle at which input pulses arrives (i.e., CVS phases). After 20 input pulses (136 seconds) these phases become constant, indicating that the oscillator is synchronized to its inputs.

[Figure 1 about here.]

[Figure 2 about here.]

[Figure 3 about here.]

2.1.2 2-to-1 synchronization at the second harmonic

Next we show that an oscillator running at the second harmonic of its input frequency can also synchronize to its inputs (see Faster Oscillator in Section 4.1). Figures 4-6 are as Figures 1-3 but for this faster oscillator. Figure 5 shows that each other oscillation cycle is precisely synchronized with the inputs (i.e., 2-1 synchronization). Figure 6 again shows that synchronization takes time to develop; for this faster oscillator the establishment of synchronization took around 80 input pulses (544 seconds).

[Figure 4 about here.]

[Figure 5 about here.]

[Figure 6 about here.]

2.2 Synchronization of neural populations to rhythmically produced CVSs

Here we demonstrate the synchronization of neural populations to rhythmically produced CVSs using ECoG recordings from electrode 136 (Figure 7) in a CVS-production session. Recording details are given in Bouchard et al. (2013). In Section 2.3 we describe this synchronization across all electrodes in the grid. We first study synchronization in oscillators running at the median CVS-production frequency (fundamental frequency; Section 2.2.1), and then in oscillators running at the twice this frequency (second-harmonic; Section 2.2.2).

[Figure 7 about here.]

2.2.1 1-to-1 synchronization at the fundamental frequency

The black curve in Figures 8 and 9 plots voltages from electrode 136 bandpass filtered around the median CVS-production frequency at the beginning and the middle of the CVS-production session, respectively. Red vertical lines mark times of initiation of CVSS productions, and black vertical lines mark peaks in voltage traces. By the middle of the CVS-production session (Figure 9), but not at the beginning of this session (Figure 8), CVSS initiations occur at precise times after filtered-voltage peaks (i.e., red vertical lines appear at similar delays after black vertical lines), and filtered-voltage peaks and CVS initiations are in a 1-to-1 correspondence (i.e., red vertical lines are matched to black vertical lines; 1-to-1 synchronization).

[Figure 8 about here.]

[Figure 9 about here.]

For each CVS production we measured the phase of the filtered voltage at which the CVS was initiated (i.e., the CVS phase). Figure 10 plots these phases across the CVS-production session. After an initial transient period of around 200 seconds, CVS phases become very precise. To quantify this precision we measured the Phase Locking Index (PLI, Section 4.4) of these phases in the interval [400-700] seconds of the CVS-production session. We obtained a PLI=0.78, which was significantly different from chance ($p < 1 \times 10^{-4}$, Rayleigh non-uniformity test). The mean phase (mean direction, Section 4.3) in this interval is indicated by the red horizontal line in Figure 10.

[Figure 10 about here.]

Figure 11 plots the running ratio of the number of CVS initiations to the number of filtered-voltage peaks in windows containing 20 CVS initiations and filtered-voltage peaks. After an initial transient period of around 200 seconds most windows show a ratio of 1.0, indicating that CVS initiations were paired with filtered-voltage peaks (i.e., 1-to-1 synchronization).

[Figure 11 about here.]

2.2.2 2-to-1 synchronization at the second harmonic

We bandpass filtered the ECoG recordings around the second CVS-production frequency harmonic. Figures 12 and 13 are as Figures 8 and 9, but for voltages filtered around the second CVS-production frequency harmonic. Again we see that around 345 seconds in the CVS-production session (Figure 13), but not at the beginning of this session (Figure 12), the filtered-voltage oscillations are precisely synchronized to the initiations of CVS. Similarly to Figure 5, Figure 13 shows that each other oscillation is synchronized to the initiation of a CVS (i.e., 2-to-1 synchronization).

[Figure 12 about here.]

[Figure 13 about here.]

Figure 14 is as Figure 10 but for voltages filtered around the second harmonic of the CVS-production frequency. CVS phases were significantly concentrated around zero (PLI=0.56; $p < 1 \times 10^{-4}$ Rayleigh non-uniformity test).

[Figure 14 about here.]

Figure 15 is as Figure 11 but for voltages filtered around the second harmonic of the CVS-production frequency. After an initial transient period of 200 seconds, for the majority of time windows, the ratio of the number of CVSS initiations to the number of filtered-voltage peaks is 0.5, indicating that, as in Figure 13, each CVS initiation is paired to two peaks of filtered voltages (i.e., 2-to-1 synchronization).

[Figure 15 about here.]

2.3 Synchronization of traveling waves to rhythmically produced consonant-vowel syllables

The previous section showed that **CVS phases** of voltages from electrode 136 were highly concentrated. Section 2.3.1 below demonstrates that this high concentration extends across most electrodes in the grid, and shows that **CVS phases** are spatially organized consistently with the propagation of **TWs**. Using this spatial organization, Section 2.3.2 isolates an extended **TW** in voltages filtered around the median **CVS**-production frequency moving from primary auditory cortex to premotor cortex, and a **TW** in coupled high-gamma amplitude moving along the same path **TW** but in opposite direction.

2.3.1 Synchronization of oscillators across electrodes

Figure 16 shows histograms of **CVS phases** for voltages filtered around the median **CVS**-production frequency between 340 and 400 seconds of the **CVS**-production session. In those histograms with high concentration of **CVS phases** (i.e., $PLI > 0.5$), a red segment indicates the mean phase (i.e., mean direction, Section 4.3). In most histograms the distribution of **CVS phases** is highly concentrated and their mean phase orderly shifts from one electrode to its neighbors (i.e., red segments change smoothly across the electrode grid).

The mean **CVS phase** should decrease as we move from one electrode to the next along the propagation direction of a **TW**. That is, in the **CVS phase** histograms the red segment should move clockwise as we move along the direction of propagation of a **TW**. The yellow arrows in Figure 16 join neighboring histograms with a high **CVS phase** concentration and point in the direction consistent with the propagation of a **TW**.

Histograms with a high **CVS phase** concentration are located in primary auditory cortex (bottom right), in the ventral sensorimotor cortex (center middle), and in the premotor cortex (top left) and **TWs** can be found between these areas, as illustrated next.

[Figure 16 about here.]

2.3.2 TWs between premotor and primary auditory cortex synchronized to the production of CVSs

Figure 17 depicts a subsets of the arrows in Figure 16 pointing along a path, from primary auditory cortex (electrode 54) to premotor cortex (electrode 174), with consistent direction of propagation of a **TW**. At the beginning of this path in electrode 54 the mean **CVS phase** is close to $3/4\pi$. Consistently with the propagation of a **TW**, the mean **CVS phase** decrease progressively along the path until electrode 174, where the mean **CVS phase** is close to $-\pi$. That is, the wave traveled almost a full cycle from auditory to premotor cortex. The video at <https://youtu.be/CkQCau8RKvI> depicts voltages filtered around the median **CVS**-production frequency at the electrodes in this path. A **TW** moving from primary auditory to premotor cortex is evident.

[Figure 17 about here.]

Using the same recordings as those characterized here, in [Rapela \(2016\)](#) we reported **TWs** in voltages filtered around the median **CVS**-production frequency and described a peculiar organization of the coupling between phases of the filtered voltages and high-gamma amplitudes. We showed that this phase-amplitude coupling led to **TWs** of coupled high-gamma amplitude moving along the same path, but in opposite direction, as **TWs** of voltages filtered around the median **CVS**-production frequency. The video at <https://youtu.be/8pd16i7jnbw> shows a **TW** of coupled high-gamma amplitude moving in the opposite direction as the **TW** shown in the previous video. Both **TWs** were extracted from a middle section of the **CVS**-production session (between 340 and 400 seconds from the start of the session).

It took several minutes from the start of the **CVS**-production session for the establishment of **TWs**. The videos at <https://youtu.be/NDrmVZ9lg9E> and at https://youtu.be/n_4KWwRkfbQ show voltages filtered around the median **CVS**-production frequency and coupled high-gamma amplitudes, respectively, extracted from the initial section of the **CVS**-production section. **TWs** in this initial section are weaker than those in the middle section of this session.

3 Discussion

In **ECoG** recordings from speech processing brain regions of a subject rhythmically producing **CVSs** here we reported that neural oscillators were precisely synchronized to the production of **CVSs** (Section 2.2). We observed that the phase of the oscillator cycle at which **CVSs** were initiated changed systematically across the grid of electrodes, consistently with the propagation of **TWs** (Section 2.3.1). Using these synchronized phases we isolated a first **TW** in voltages filtered around the median **CVS**-production frequency moving from premotor to primary auditory cortex, and a second **TW** in high-gamma amplitude coupled to phase at the **CVS**-production frequency moving along the same path as the previous **TW** but in opposite direction (Section 2.3.2). These **TWs** may constitute a neural mechanisms for the interaction between the production of speech and the perception of self-generated speech.

The observed synchronization of the initiation of **CVS** productions and **TWs** is not a direct consequence of the rhythmic **CVS**-production task, since it took several minutes for the establishment of this synchronization (Figures 10 and 14) and the synchronization was observed at the second harmonic of the **CVS**-production frequency (Figures 13 and 14).

After an initial transient period of around 4 minutes, we observed precise synchronization of oscillators across most electrodes of the array (Figure 16). Future studies need to investigate how this extended synchronization is achieved. Could it be the case that exists an input (e.g., from Brocca’s area) to a small group of oscillators that synchronizes them to the production of **CVSs**, and that later the synchronization spreads to most electrodes in the array by weak coupling between oscillators?

4 Methods

4.1 Oscillator models

In Section 2.1 we used the Persistent Sodium Potassium model (INaPK; [Izhikevich, 2007](#)). The parameters of the slower oscillator in Section 2.1.1 were as those in Figure 4.1a of [Izhikevich \(2007\)](#) with a constant input current $I = 10$, and those of the faster oscillator in Section 2.1.2 were as those in Figure 4.1b of [Izhikevich \(2007\)](#) with a constant input current $I = 50$.

4.2 Measuring CVS phases

A **CVS phase** measures in radians the location in an oscillatory cycle of filtered voltages where the production of a **CVS** is initiated. Call t_{CVS} the time of initiation of a **CVS**, t_{peak} the time of the peak of filtered voltages closest to t_{CVS} , t_{next} the time of the first peak following the one at t_{peak} , and t_{prev} the time of the first peak preceding the one at t_{peak} . We defined

$$\text{CVS phase}(t_{CVS}) = \frac{t_{CVS} - t_{peak}}{k} \quad (1)$$

If $t_{CVS} > t_{peak}$ then we used a normalization constant k so that $\text{CVS Phase}(t_{next}) = 2\pi$ (i.e., $k = \frac{t_{next} - t_{peak}}{2\pi}$), and if $t_{CVS} < t_{peak}$ then we took a normalization constant k so that $\text{CVS phase}(t_{next}) = -2\pi$ (i.e., $k = \frac{t_{peak} - t_{prev}}{2\pi}$).

4.3 Circular statistics concepts

This section introduces concepts from circular statistics (Fisher, 1996) used to define **PLI** in Section 4.4. Given a set of circular variables (e.g., phases), $\theta_1, \dots, \theta_N$, we associate to each circular variable a two-dimensional unit vector. Using notation from complex numbers, the unit vector associated with variable θ_i is:

$$vec(\theta_i) = e^{j\theta_i} \quad (2)$$

The *resultant vector*, \mathbf{R} , is the sum of the associated unit vectors:

$$\mathbf{R}(\theta_1, \dots, \theta_N) = \sum_{i=1}^N vec(\theta_i) \quad (3)$$

The *mean resultant length*, \bar{R} , is the length of the resultant vector divided by the number of circular variables:

$$\bar{R}(\theta_1, \dots, \theta_N) = \frac{1}{N} |\mathbf{R}(\theta_1, \dots, \theta_N)| \quad (4)$$

The *circular variance*, CV , is one minus the mean resultant length:

$$CV(\theta_1, \dots, \theta_N) = 1 - \bar{R}(\theta_1, \dots, \theta_N) \quad (5)$$

The *mean direction*, $\bar{\theta}$, is the angle of the resultant vector:

$$\bar{\theta}(\theta_1, \dots, \theta_N) = \arg(\mathbf{R}(\theta_1, \dots, \theta_N)) \quad (6)$$

Note that the mean direction is not defined when the resultant vector is zero, since the angle of the zero vector is undefined.

4.4 PLI

The **PLI**, also known as inter-trial coherence (ITC), is a measure of coherence among a set of phases $\theta_1, \dots, \theta_n$ (Tallon Baudry et al., 1996; Delorme and Makeig, 2004). It is the mean resultant length (\bar{R} , Eq. 4) of these phases:

$$PLI(\theta_1, \dots, \theta_N) = \bar{R}(\theta_1, \dots, \theta_N) \quad (7)$$

5 Acknowledgments

We thank Dr. Edward Chang and Dr. Kristofer Bouchard for sharing the **ECoG** recordings.

References

- J. Besle, C.A. Schevon, A.D. Mehta, P. Lakatos, R.R. Goodman, G.M. McKhann, R.G. Emerson, and C.E. Schroeder. Tuning of the human neocortex to the temporal dynamics of attended events. *The Journal of Neuroscience*, 31(9):3176–3185, 2011.
- K.E. Bouchard, N. Mesgarani, K. Johnson, and E.F. Chang. Functional organization of human sensorimotor cortex for speech articulation. *Nature*, 495:327–332, 2013.
- A.M. Cravo, G. Rohenkohl, V. Wyart, and A.C. Nobre. Temporal expectation enhances contrast sensitivity by phase entrainment of low-frequency oscillations in visual cortex. *The Journal of Neuroscience*, 33(9):4002–4010, 2013.
- F. Cummins. Oscillators and syllables: a cautionary note. *Frontiers in Psychology*, 3:364, 2012.
- Louis J DeFelice and Aurora Isaac. Chaotic states in a random world: Relationship between the nonlinear differential equations of excitability and the stochastic properties of ion channels. *Journal of Statistical Physics*, 70(1):339–354, 1993.
- A. Delorme and S. Makeig. EEGLAB: an open source toolbox for analysis of single-trial EEG dynamics including independent component analysis. *Journal of Neuroscience Methods*, 134(1): 9–21, 2004.
- N. Ding and J.Z. Simon. Cortical entrainment to continuous speech: functional roles and interpretations. *Front. Hum. Neurosci*, 8(311):10–3389, 2014.
- Keith B Doelling, Luc H Arnal, Oded Ghitza, and David Poeppel. Acoustic landmarks drive delta–theta oscillations to enable speech comprehension by facilitating perceptual parsing. *Neuroimage*, 85:761–768, 2014.
- N.I. Fisher. *Statistical analysis of circular data*. Cambridge University Press, Cambridge, UK, 1996.
- Robert Galambos, Scott Makeig, and Peter J Talmachoff. A 40-hz auditory potential recorded from the human scalp. *Proceedings of the National Academy of Sciences*, 78(4):2643–2647, 1981.
- L. Glass. Synchronization and rhythmic processes in physiology. *Nature*, 410:227–284, 2001.
- Martin Golubitsky, Ian Stewart, Pietro-Luciano Buono, and JJ Collins. Symmetry in locomotor central pattern generators and animal gaits. *Nature*, 401(6754):693–695, 1999.
- M. Gomez-Ramirez, S.P. Kelly, S. Molholm, P. Sehatpour, T.H. Schwartz, and J.J. Foxe. Oscillatory sensory selection mechanism during intersensory attention to rhythmic auditory and visual inputs: a human electrocorticographic investigation. *The Journal of Neuroscience*, 31(50): 18556–18567, 2011.
- CARL Graves, LEON Glass, DONALD Laporta, ROGER Meloche, and ALEX Grassino. Respiratory phase locking during mechanical ventilation in anesthetized human subjects. *American Journal of Physiology-Regulatory, Integrative and Comparative Physiology*, 250(5):R902–R909, 1986.
- Michael J Gray, Hans-Peter Frey, Tommy J Wilson, and John J Foxe. Oscillatory recruitment of bilateral visual cortex during spatial attention to competing rhythmic inputs. *The Journal of Neuroscience*, 35(14):5489–5503, 2015.

- J. Gross, N. Hoogenboom, G. Thut, P. Schyns, S. Panzeri, P. Belin, and S. Garrod. Speech rhythms and multiplexed oscillatory sensory coding in the human brain. *PLoS Biology*, 11(12), 2013. doi: 10.1371/journal.pbio.1001752.
- Michael R Guevara and Timothy J Lewis. A minimal single-channel model for the regularity of beating in the sinoatrial node. *Chaos: An Interdisciplinary Journal of Nonlinear Science*, 5(1): 174–183, 1995.
- Eugene M. Izhikevich. *Dynamical systems in neuroscience*. MIT press, 2007.
- P. Lakatos, A.S. Shah, K.H. Knuth, I. Ulbert, G. Kamos, and C.E. Schroeder. An oscillatory hierarchy controlling neural excitability and stimulus processing in the auditory cortex. *J. Neurophysiology*, 94(3):1904–1911, 2005.
- P. Lakatos, G. Kamos, A.D. Mehta, I. Ulbert, and C.E. Schroeder. Entrainment of neuronal oscillations as a mechanism of attentional selection. *Science*, 320:110–113, 2008.
- P. Lakatos, G. Musacchia, M.N. O’connel, A.Y. Falchier, D.C. Javitt, and C.E. Schroeder. The spectrotemporal filter mechanism of auditory selective attention. *Neuron*, 77(4):750–761, 2013.
- K.E. Mathewson, M. Fabiani, G. Gratton, D.M. Beck, and A. Lleras. Rescuing stimuli from invisibility: Inducing a momentary release from visual masking with pre-target entrainment. *Cognition*, 115:186–191, 2010.
- R.E. Millman, S.R. Johnson, and G. Prendergast. The role of phase-locking to the temporal envelope of speech in auditory perception and speech intelligibility. *Journal of Cognitive Neuroscience*, 2015.
- M.N. O’Connell, A. Falchier, T. McGinnis, C.E. Schroeder, and P. Lakatos. Dual mechanism of neuronal ensemble inhibition in primary auditory cortex. *Neuron*, 69(4):805–817, 2011.
- Hyojin Park, Robin AA Ince, Philippe G Schyns, Gregor Thut, and Joachim Gross. Frontal top-down signals increase coupling of auditory low-frequency oscillations to continuous speech in human listeners. *Current Biology*, 2015.
- J.E. Pelle and M.H. Davis. Neural oscillations carry speech rhythm through to comprehension. *Front Psychol*, 3(320):1–17, 2012.
- GA Petrillo and LEON Glass. A theory for phase locking of respiration in cats to a mechanical ventilator. *American Journal of Physiology-Regulatory, Integrative and Comparative Physiology*, 246(3):R311–R320, 1984.
- Joaquín Rapela. Entrainment of traveling waves to rhythmic motor acts, 2016. URL <http://arxiv.org/abs/1606.02372>.
- D Regan. Some characteristics of average steady-state and transient responses evoked by modulated light. *Electroencephalography and clinical neurophysiology*, 20(3):238–248, 1966.
- Peggy M Simon, Alfred M Habel, J Andrew Daubenspeck, and JC Leiter. Vagal feedback in the entrainment of respiration to mechanical ventilation in sleeping humans. *Journal of Applied Physiology*, 89(2):760–769, 2000.
- E. Spaak, F.P. de Lange, and O Jensen. Local entrainment of alpha oscillations by visual stimuli causes cyclic modulation of perception. *J Neurosci*, 34(10):3536–44, 2014.
- S.H. Strogatz. *The mathematical structure of the human sleep-wake cycle*, volume 86. Springer, 1986.

- C. Tallon Baudry, O. Bertrand, C. Delpuech, and J. Pernier. Stimulus specificity of phase-locked and non-phase-locked 40 hz visual responses in human. *The Journal of Neuroscience*, 16:4240–4349, 1996.
- Arthur T Winfree. *The geometry of biological time*, volume 12. Springer Science & Business Media, 2001.
- E.M. Zion Golumbic, D. Poeppel, and C.E. Schroeder. Temporal context in speech processing and attentional stream selection: a behavioral and neural perspective. *Brain and language*, 122(3): 151–161, 2012.
- E.M. Zion Golumbic, N. Ding, S. Bickel, P. Lakatos, C.A. Schevon, G.M. McKhann, R.R. Goodman, R. Emerson, A.D. Mehta, J.Z. Simon, D. Poeppel, and C.E. Schroeder. Mechanisms underlying selective neuronal tracking of attended speech at a “cocktail party”. *Neuron*, 77(5):980–991, 2013.
- E.M. Zion Golumbic, N. Ding, S. Bickel, P. Lakatos, C.A. Schevon, G.M. McKhann, R.R. Goodman, R. Emerson, A.D. Mehta, J.Z. Simon, D. Poeppel, and C.E. Schroeder. Mechanisms underlying selective neuronal tracking of attended speech at a cocktail party. *Neuron*, 77(5):980–991, 2013.

List of Figures

1	Lack of synchronization of a single-neuron model to periodic rhythmic stimulation at the beginning of the stimulation period. Before stimulation the neural model was running on a limit cycle with frequency close to that of stimulation.	12
2	Precise synchronization of a single-neuron model to periodic rhythmic stimulation after 160 seconds of stimulation. Before stimulation the neural model was running on a limit cycle with frequency close to that of stimulation. . . .	13
3	Temporal evolution of synchronization across time. Blue points indicate the phase of the spiking cycle at which current inputs were delivered. Before stimulation the neural model was running on a limit cycle with frequency close to that of stimulation.	14
4	Lack of synchronization of a single-neuron oscillator model to rhythmic stimulation at the beginning of the stimulation period. Before stimulation the model was running on a limit cycle at the second harmonic of the stimulation frequency.	15
5	Precise synchronization of a single-neuron oscillator model to rhythmic stimulation by 640 seconds in the stimulation period. Before stimulation the neural model was running on a limit cycle at the second harmonic of the stimulation frequency.	16
6	Temporal evolution of synchronization for a single-neuron oscillator model running on a limit cycle at the second harmonic of the stimulation frequency. Blue points indicate phases of the spiking cycle at which current input pulses were delivered to the model.	17
7	Grid of ECoG electrodes superimposed on an MRI reconstruction of the subjects' brain.	18
8	At the beginning of the CVS-production session, voltages from electrode 136 filtered around the CVS-production frequency are not synchronized to CVS initiations. The black trace plots the filtered voltage, vertical black lines appear at peaks of the filtered voltage, and vertical red lines indicate times of initiation of CVS productions.	19
9	Around 340 seconds into the CVS-production session almost perfect synchronization is achieved between CVSs initiations and voltages from electrode 136 filtered around the median CVS-production frequency. Same format as in Figure 8.	20
10	Temporal evolution of synchronization between CVS initiations and voltages from electrode 136 filtered around the median CVS-production frequency. Points indicate the phase of the filtered-voltage oscillation at which CVSs were initiated (i.e., CVS phases). After an initial transient of around 200 seconds, CVSs tend to be initiated at a fixed phase of the filtered-voltage oscillations. Between 400 seconds and the end of the CVS-production session, CVS phases are highly concentrated ($PLI=0.78$; $p < 1 \times 10^{-4}$, Rayleigh non-uniformity test). The mean CVS phase (mean direction, Section 4.3) in this period is less than $\pi/2$ (red horizontal line).	21

11	After an initial transient period of around 200 seconds, a 1-to-1 synchronization developed between the initiations of CVSs and filtered voltages from electrode 136. Voltages were filtered around the median CVS -production frequency. Points give the ratio between the number of CVS initiations and the number of peaks in the filtered voltage in a sliding window containing 20 CVS initiations and filtered-voltage peaks. After the transient period, most ratios take the value 1.0, indicating that one filtered-voltage peak is paired with one CVS initiation (i.e, 1-to-1 synchronization).	22
12	At the beginning of the CVS -production session no synchronization is apparent between CVS initiations and peaks of voltages from electrode 136 filtered around the second harmonic of the CVS -production frequency. Same format as in Figure 8.	23
13	By 340 seconds into the CVS -production session an almost perfect synchronization develops between the initiation of CVSs and voltages from electrode 136 filtered around the second harmonic of the median CVS -production frequency. The synchronization is 2-to-1 (two filtered-voltage oscillations are paired with one CVS initiation). Same format as in Figure 8. The green vertical lines mark peaks of filtered voltages not paired to CVS initiations. .	24
14	Temporal evolution of synchronization between CVS initiations and voltage peaks from electrode 136 filtered around the second harmonic of the CVS -production frequency. Same format as in Figure 10. After an initial transient period of around 200 seconds, CVSs tend to be initiated at peaks of the filtered-voltage oscillations (CVS phase =0). Between 400 seconds and the end of the CVS -production session, CVS phases are highly concentrated (PLI =0.56; $p < 1 \times 10^{-4}$, Rayleigh non-uniformity test) around the filtered-voltages peaks. The mean CVS phase (mean direction, Section 4.3) in this period is close to zero (red horizontal line).	25
15	After an initial transient period of around 200 second, a 2-to-1 synchronization developed between the initiation of CVSs and voltages filtered at the second harmonic of the CVS -production frequency. Same format as in Figure 11. After the initial transient period most ratios take the value 0.5, indicating that two filtered-voltage peaks were paired with one CVS initiation (i.e., 2-to-1 synchronization).	26
16	Histograms of CVS phases for all electrodes in the grid. Red segments are drawn at the mean CVS phase (mean direction, Section 4.3) in histograms with high CVS phase concentration (PLI >0.5, Section 4.4). CVS phases should decrease between one electrode and the next along the direction of propagation of a TW (i.e., red segments should move in the clockwise direction). Yellow arrows joining neighbor electrodes point in the direction consistent with the propagation of a TW . The title of each histogram gives the electrode number, the PLI , and the p-value of a Rayleigh non-uniformity test. Histograms with high concentration of CVS phases are mostly located in the auditory cortex (bottom right), ventral sensorimotor cortex (center middle), and premotor cortex (top left), and TWs can be found between some of these areas (e.g., Figure 17).	27
17	Histograms of CVS phase gradients for all electrodes in the grid showing a subset of the arrows in Figure 16 pointing in the direction of propagation of a TW from primary auditory cortex (electrode 54) to premotor cortex (electrode 174). Same format as in Figure 16.	28

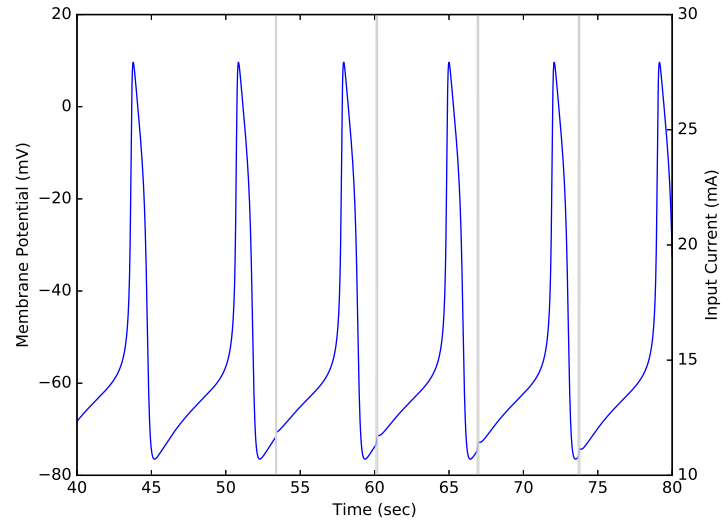


Figure 1: Lack of synchronization of a single-neuron model to periodic rhythmic stimulation at the beginning of the stimulation period. Before stimulation the neural model was running on a limit cycle with frequency close to that of stimulation.

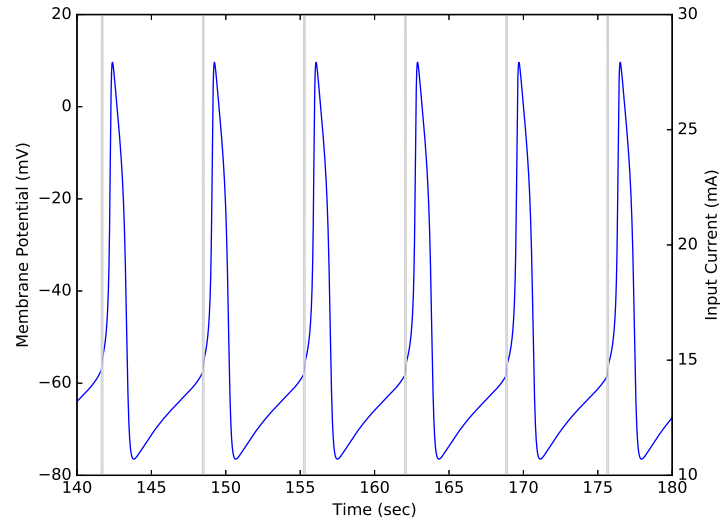


Figure 2: Precise synchronization of a single-neuron model to periodic rhythmic stimulation after 160 seconds of stimulation. Before stimulation the neural model was running on a limit cycle with frequency close to that of stimulation.

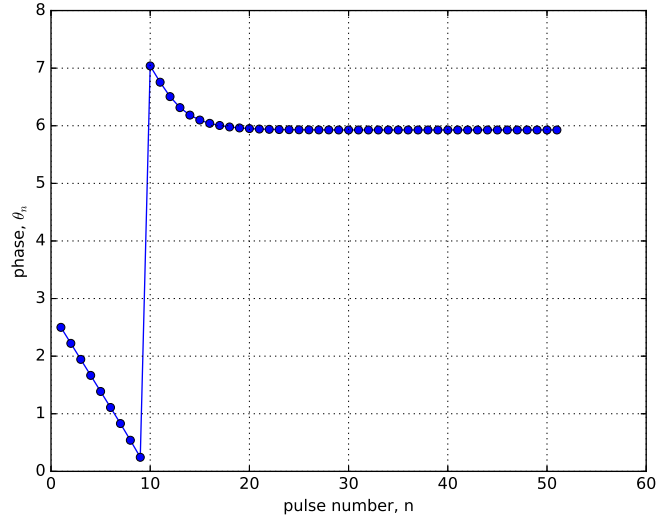


Figure 3: Temporal evolution of synchronization across time. Blue points indicate the phase of the spiking cycle at which current inputs were delivered. Before stimulation the neural model was running on a limit cycle with frequency close to that of stimulation.

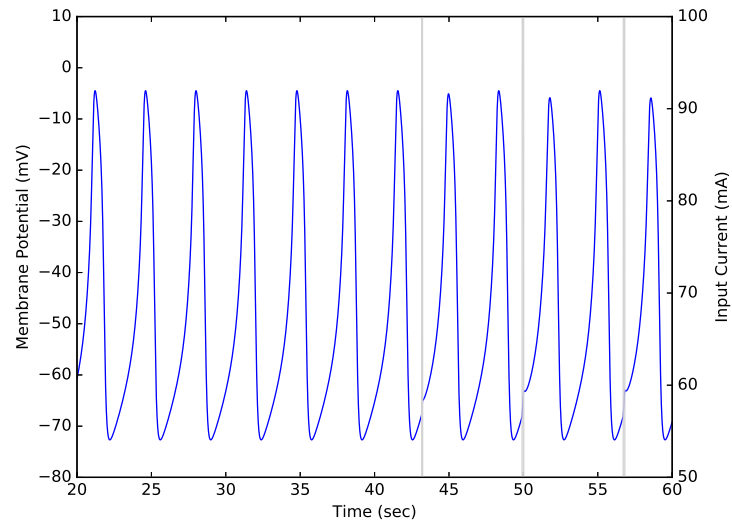


Figure 4: Lack of synchronization of a single-neuron oscillator model to rhythmic stimulation at the beginning of the stimulation period. Before stimulation the model was running on a limit cycle at the second harmonic of the stimulation frequency.

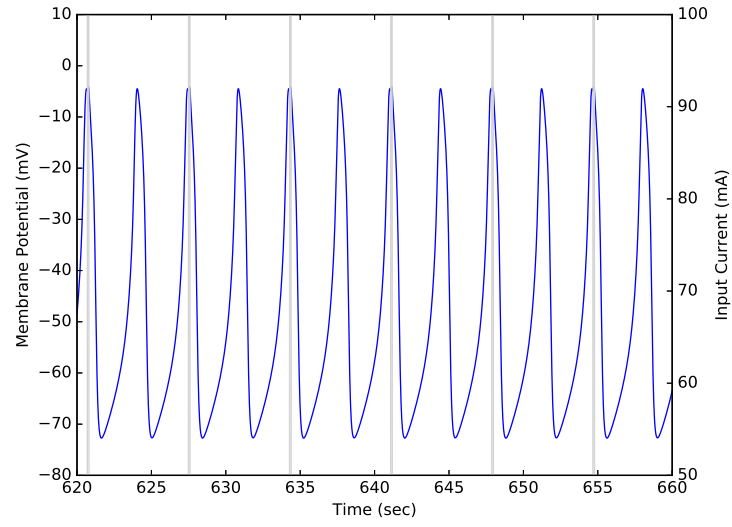


Figure 5: Precise synchronization of a single-neuron oscillator model to rhythmic stimulation by 640 seconds in the stimulation period. Before stimulation the neural model was running on a limit cycle at the second harmonic of the stimulation frequency.

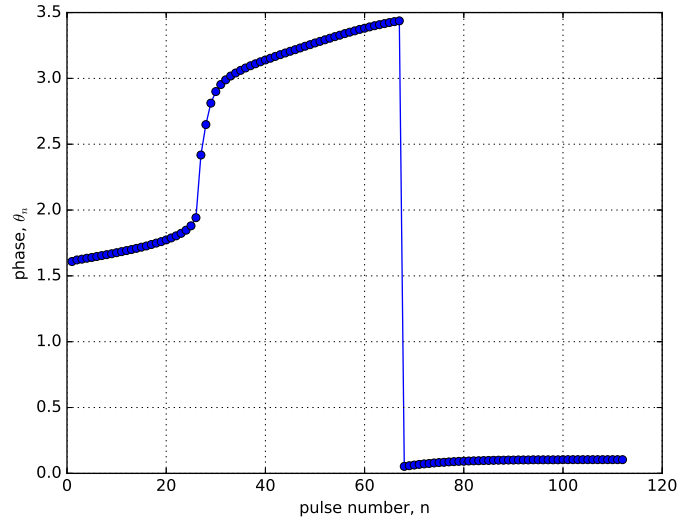


Figure 6: Temporal evolution of synchronization for a single-neuron oscillator model running on a limit cycle at the second harmonic of the stimulation frequency. Blue points indicate phases of the spiking cycle at which current input pulses were delivered to the model.

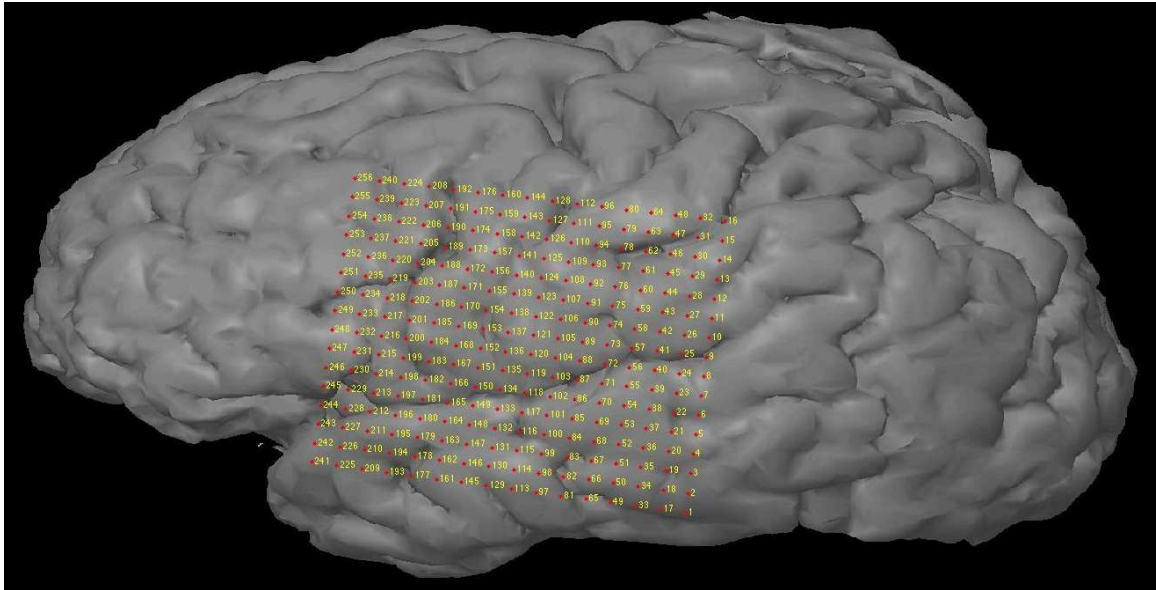


Figure 7: Grid of ECoG electrodes superimposed on an MRI reconstruction of the subjects' brain.

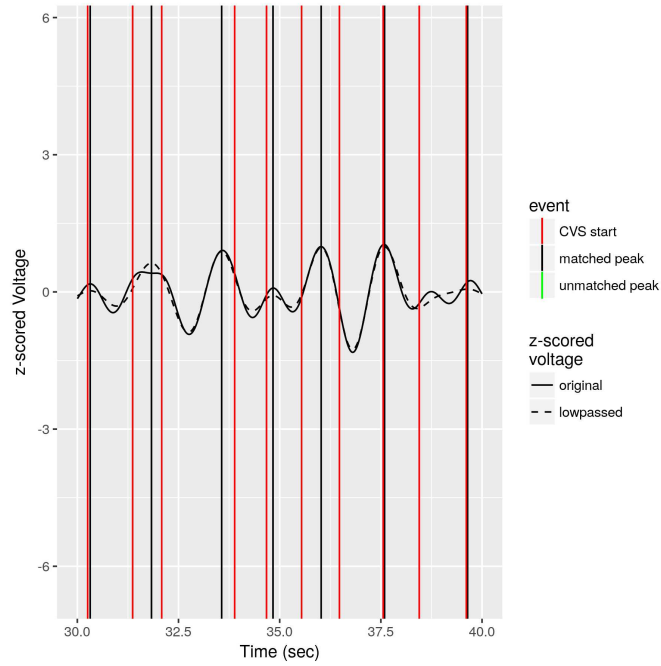


Figure 8: At the beginning of the **CVS**-production session, voltages from electrode 136 filtered around the **CVS**-production frequency are not synchronized to **CVS** initiations. The black trace plots the filtered voltage, vertical black lines appear at peaks of the filtered voltage, and vertical red lines indicate times of initiation of **CVS** productions.

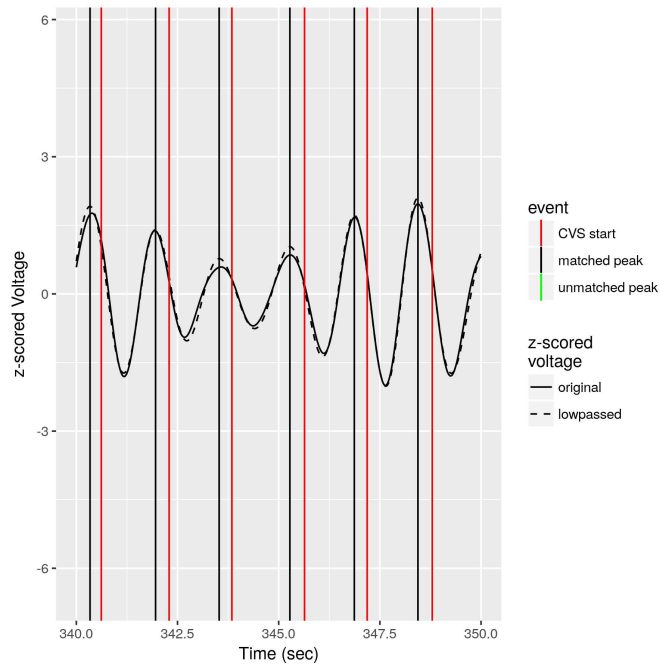


Figure 9: Around 340 seconds into the **CVS**-production session almost perfect synchronization is achieved between **CVSs** initiations and voltages from electrode 136 filtered around the median **CVS**-production frequency. Same format as in Figure 8.

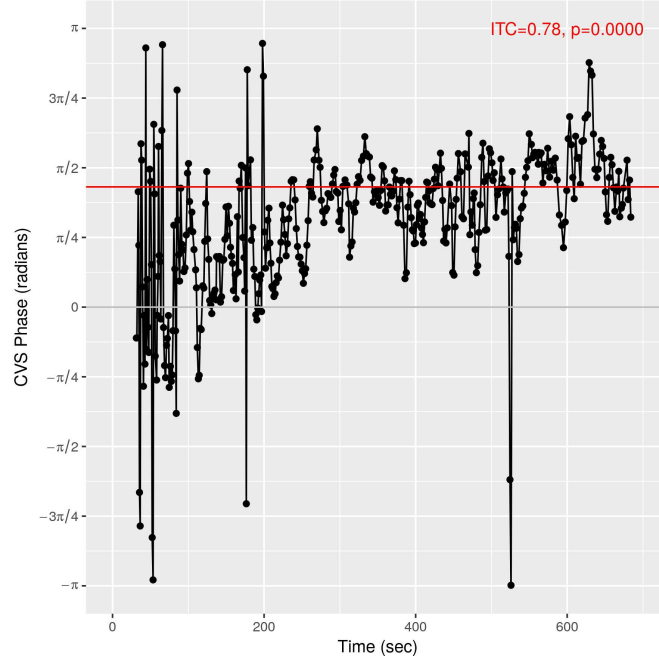


Figure 10: Temporal evolution of synchronization between **CVS** initiations and voltages from electrode 136 filtered around the median **CVS**-production frequency. Points indicate the phase of the filtered-voltage oscillation at which **CVSs** were initiated (i.e., **CVS phases**). After an initial transient of around 200 seconds, **CVSs** tend to be initiated at a fixed phase of the filtered-voltage oscillations. Between 400 seconds and the end of the **CVS**-production session, **CVS phases** are highly concentrated (**PLI**=0.78; $p < 1 \times 10^{-4}$, Rayleigh non-uniformity test). The mean **CVS phase** (mean direction, Section 4.3) in this period is less than $\pi/2$ (red horizontal line).

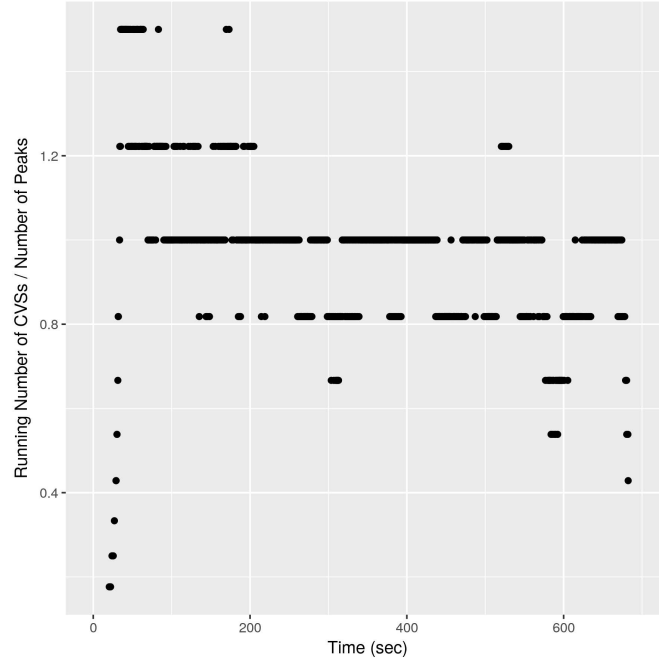


Figure 11: After an initial transient period of around 200 seconds, a 1-to-1 synchronization developed between the initiations of **CVSs** and filtered voltages from electrode 136. Voltages were filtered around the median **CVS**-production frequency. Points give the ratio between the number of **CVS** initiations and the number of peaks in the filtered voltage in a sliding window containing 20 **CVS** initiations and filtered-voltage peaks. After the transient period, most ratios take the value 1.0, indicating that one filtered-voltage peak is paired with one **CVS** initiation (i.e, 1-to-1 synchronization).

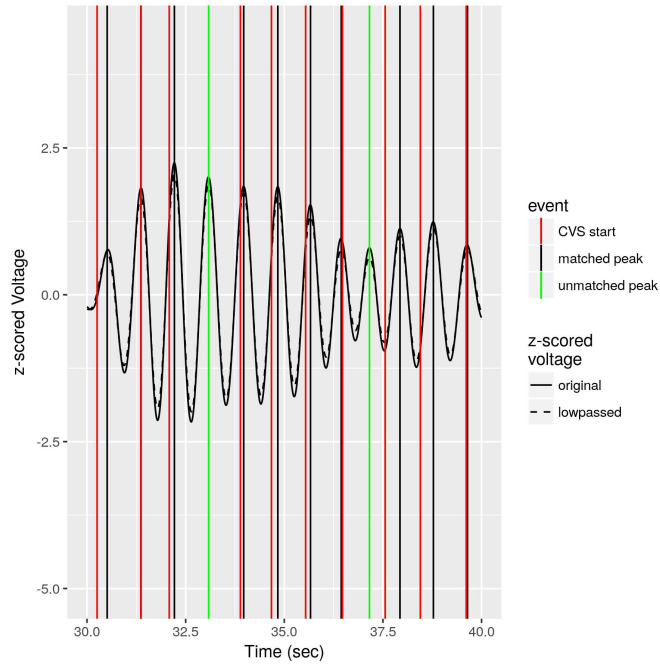


Figure 12: At the beginning of the **CVS**-production session no synchronization is apparent between **CVS** initiations and peaks of voltages from electrode 136 filtered around the second harmonic of the **CVS**-production frequency. Same format as in Figure 8.

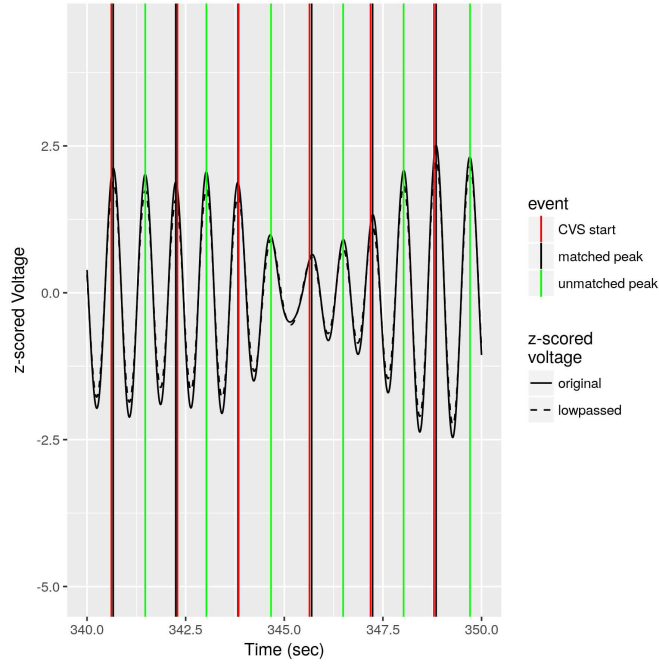


Figure 13: By 340 seconds into the **CVS**-production session an almost perfect synchronization develops between the initiation of **CVSs** and voltages from electrode 136 filtered around the second harmonic of the median **CVS**-production frequency. The synchronization is 2-to-1 (two filtered-voltage oscillations are paired with one **CVS** initiation). Same format as in Figure 8. The green vertical lines mark peaks of filtered voltages not paired to **CVS** initiations.

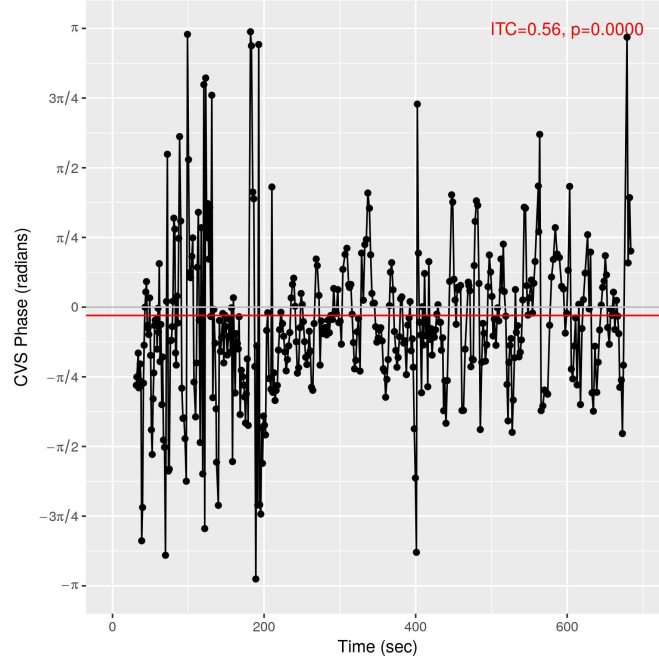


Figure 14: Temporal evolution of synchronization between **CVS** initiations and voltage peaks from electrode 136 filtered around the second harmonic of the **CVS**-production frequency. Same format as in Figure 10. After an initial transient period of around 200 seconds, **CVSs** tend to be initiated at peaks of the filtered-voltage oscillations (**CVS phase**=0). Between 400 seconds and the end of the **CVS**-production session, **CVS phases** are highly concentrated (**PLI**=0.56; $p < 1 \times 10^{-4}$, Rayleigh non-uniformity test) around the filtered-voltages peaks. The mean **CVS phase** (mean direction, Section 4.3) in this period is close to zero (red horizontal line).

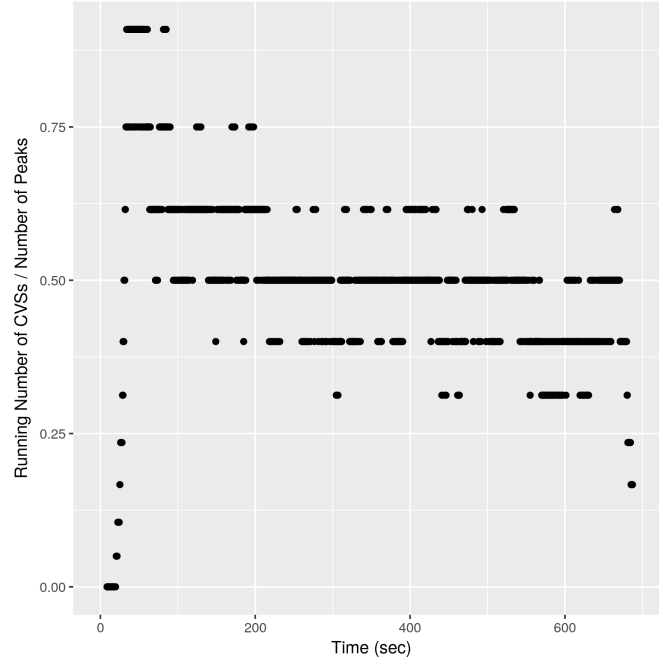


Figure 15: After an initial transient period of around 200 second, a 2-to-1 synchronization developed between the initiation of **CVSs** and voltages filtered at the second harmonic of the **CVS**-production frequency. Same format as in Figure 11. After the initial transient period most ratios take the value 0.5, indicating that two filtered-voltage peaks were paired with one **CVS** initiation (i.e., 2-to-1 synchronization).

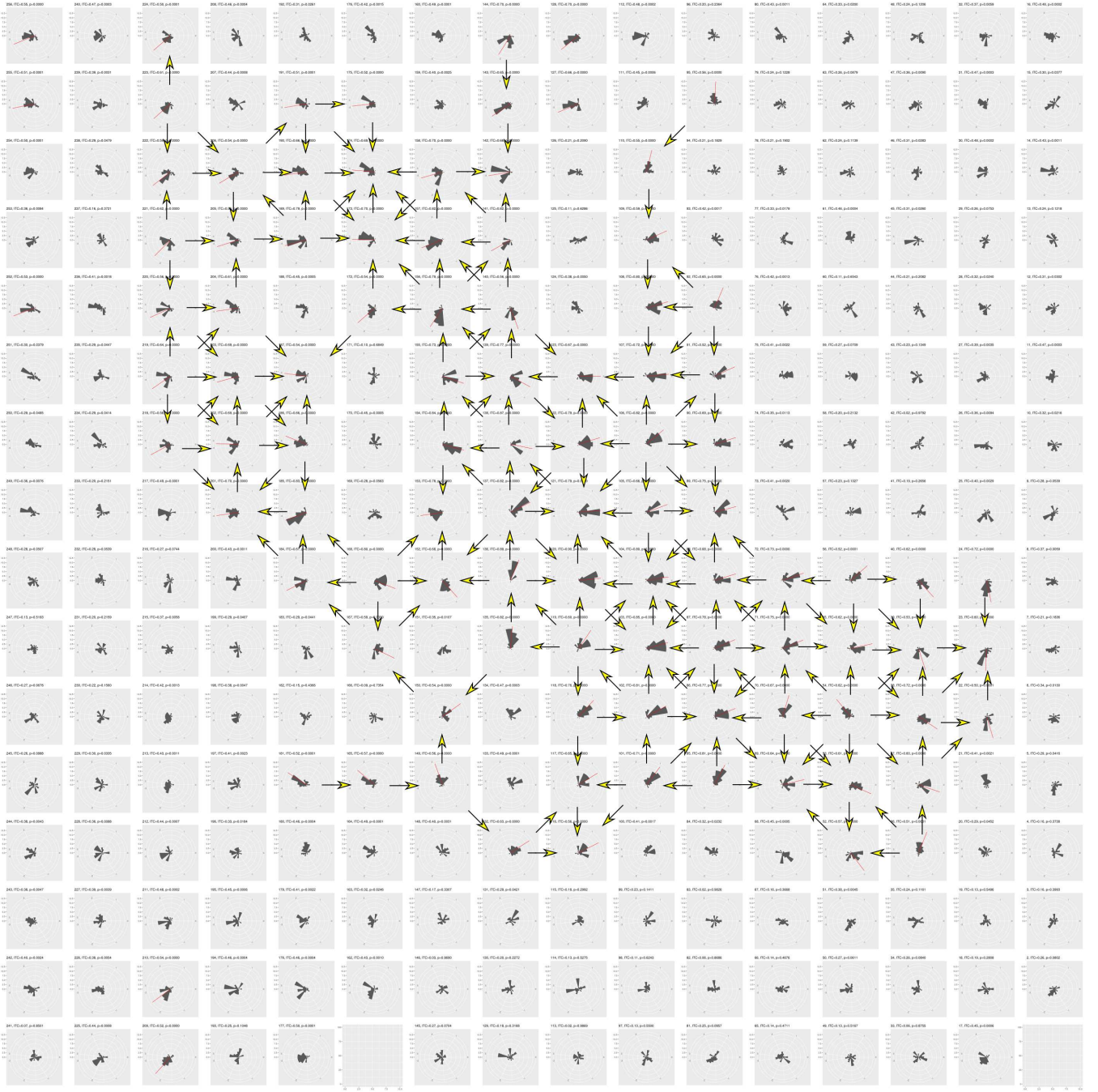


Figure 16: Histograms of **CVS phases** for all electrodes in the grid. Red segments are drawn at the mean **CVS phase** (mean direction, Section 4.3) in histograms with high **CVS phase** concentration ($PLI > 0.5$, Section 4.4). **CVS phases** should decrease between one electrode and the next along the direction of propagation of a **TW** (i.e., red segments should move in the clockwise direction). Yellow arrows joining neighbor electrodes point in the direction consistent with the propagation of a **TW**. The title of each histogram gives the electrode number, the **PLI**, and the p-value of a Rayleigh non-uniformity test. Histograms with high concentration of **CVS phases** are mostly located in the auditory cortex (bottom right), ventral sensorimotor cortex (center middle), and premotor cortex (top left), and **TWs** can be found between some of these areas (e.g., Figure 17).



Figure 17: Histograms of **CVS** phase gradients for all electrodes in the grid showing a subset of the arrows in Figure 16 pointing in the direction of propagation of a **TW** from primary auditory cortex (electrode 54) to premotor cortex (electrode 174). Same format as in Figure 16.